

Matrix cofactorization for joint spatial-spectral unmixing of hyperspectral images

Adrien Lagrange, *Student Member, IEEE*, Mathieu Fauvel, *Senior Member, IEEE*,
Stéphane May and Nicolas Dobigeon, *Senior Member, IEEE*

Abstract—Hyperspectral unmixing aims at identifying a set of elementary spectra and the corresponding mixture coefficients for each pixel of an image. As the elementary spectra correspond to the reflectance spectra of real materials, they are often very correlated yielding an ill-conditioned problem. To enrich the model and to reduce ambiguity due to the high correlation, it is common to introduce spatial information to complement the spectral information. The most common way to introduce spatial information is to rely on a spatial regularization of the abundance maps. In this paper, instead of considering a simple but limited regularization process, spatial information is directly incorporated through the newly proposed context of spatial unmixing. Contextual features are extracted for each pixel and this additional set of observations is decomposed according to a linear model. Finally the spatial and spectral observations are unmixed jointly through a cofactorization model. In particular, this model introduces a coupling term used to identify clusters of shared spatial and spectral signatures. An evaluation of the proposed method is conducted on synthetic and real data and shows that results are accurate and also very meaningful since they describe both spatially and spectrally the various areas of the scene.

Index Terms—Image analysis, spectral unmixing, hyperspectral imaging, cofactorization.

I. INTRODUCTION

OVER the past decades the huge potential of Earth observation has pushed the scientific community to develop automatic methods to extract information from the acquired data. Hyperspectral imaging is a specific image modality proposing a very rich information in the spectral domain. Each pixel is indeed a dense sampling of the reflectance spectrum of the underlying area, with usually hundreds of measurements from visible to infrared domains. The particularities of hyperspectral images have led to the development of specific interpretation methods in order to fully benefit from this spectral information. Spectral unmixing methods [1] are in particular based on the assumption that the reflectance spectrum of a pixel is the result of the mixture of a reduced set of elementary spectra called endmembers. Each of these

endmembers is the reflectance spectrum corresponding to a specific material present in the scene. An unmixing method aims at estimating the present endmembers and at recovering the proportions of each material in a given pixel collected in a so-called abundance vector. These abundance vectors allow, for example, the end-user to build abundance maps displaying the distribution of materials over the observed scene.

As hyperspectral images contain a rich spectral information, many unmixing methods focus on exploiting it and often neglect spatial information. Many well-established methods process pixels without taking in consideration the basic idea that neighboring pixels are often very similar. The only shared information between pixels is a common endmember matrix [2], [3]. Nevertheless, advanced methods have been proposed to perform spatial-spectral unmixing [4]. The most direct approach is to consider local spatial regularization of the abundance maps. Several works, such as SUnSAL-TV [5] or S2WSU [6], proposed to use TV-norm regularization to achieve this goal. Identification of clusters of spectrally similar pixels, scattered in small groups, was also used to impose spatial smoothing of the abundances, e.g., in [7]–[9]. In a different way, other works used the local neighborhood to identify the subset of endmembers present in the neighborhood. It is especially useful when dealing with a large number of endmembers [10], [11]. Finally, at a lesser extent, the spatial information has also been used to help the extraction of endmembers. Indeed, endmembers extraction is often performed before estimating the abundance vectors. Some preprocessing were proposed to ease the extraction and identification of pure pixels as the averaging of spectra over superpixels [12] or the use of spatial homogeneity scalar factors [13].

Overall it is noticeable that all these approaches tend to exploit the very simple idea that neighboring pixels should be similar. However, spatial information is richer than this simple statement. For example, two spectrally very similar pixels can be discriminated using their context, e.g. a natural grassland and a crop field are spectrally very closed but the first is spatially homogeneous when the second is organized in rows. Exploiting spatial patterns and textures descriptors is thus expected to be helpful to the unmixing process. To exploit this assumption, this paper proposes a model based on a cofactorization task to jointly infer common spatial and spectral signatures from the image.

Cofactorization methods, sometimes referred to as coupled dictionary learning, have been implemented with success in many application fields, e.g., for text mining [14], music source separation [15] and image analysis [16], [17], among

A. Lagrange and N. Dobigeon are with University of Toulouse, IRIT/INP-ENSEEIH, Toulouse, France (e-mail:{adrien.lagrange, nicolas.dobigeon}@enseeiht.fr).

M. Fauvel is with CESBIO, University of Toulouse, CNES/CNRS/INRA/IRD/UPS, Toulouse, France (e-mail:mathieu.fauvel@inra.fr).

S. May is with Centre National d'Études Spatiales (CNES), DCT/SI/AP, Toulouse, France (e-mail:stephane.may@cnes.fr).

Part of this work has been supported by Centre National d'Études Spatiales (CNES), by Occitanie Region, by EU FP7 through the ERANETMED JC-WATER program, MapInvPlnt Project ANR-15-NMED-0002-02 and by the ANR-3IA Artificial and Natural Intelligence Toulouse Institute (ANITI).

others. The main idea is to define an optimization problem relying on two factorizing models supplemented by a coupling term enforcing a dependence between the two models. The method proposed in this article, called CoFUn for cofactorization unmixing, jointly considers a spectral unmixing model and a decomposition of contextual features computed from the panchromatic image of the same scene. The coupling term is interpreted as a clustering identifying groups of pixels sharing similar spectral signatures and spatial contexts. This method exhibits two major advantages: *i*) it provides very competitive results even though the method is unsupervised (i.e., it estimates both endmember signatures and abundance maps) and *ii*) it provides very insightful results since the scene is partitioned into areas characterized by spectral and spatial signatures.

The remaining of the article is organized as follows. Section II defines the spectral and the spatial models and further discusses the joint cofactorization problem. Section III then details the optimization scheme developed to solve the resulting non-convex non-smooth minimization problem. An evaluation of the proposed joint model is then conducted first on synthetic data in Section IV and then on real data in Section V. Finally, Section VI concludes the paper and presents some research perspectives to this work.

II. TOWARDS SPATIAL-SPECTRAL UNMIXING

The main goal of this section is to introduce a model capable of spectrally and spatially characterizing an hyperspectral image. In particular, instead of incorporating prior spatial information as a regularization [5], the concept of spatial unmixing, detailed in Section II-B, is introduced alongside a conventional spectral unmixing model in order to propose a new joint framework of spatial-spectral unmixing.

A. Spectral mixing model

Spectral unmixing aims at identifying the elementary spectra and the proportion of each material in a given pixel [1]. Each of the P pixels \mathbf{y}_p is a d_1 -dimensional measurement of a reflectance spectrum and is assumed to be a combination of R_1 elementary spectra \mathbf{m}_r , called endmembers, with $R_1 \ll d_1$. The so-called abundance vector $\mathbf{a}_p \in \mathbb{R}^{R_1}$ refers to the corresponding mixing coefficients in this pixel. In a general case, where no particular assumption is made on the observed scene, the conventional linear mixture model (LMM) is widely adopted to describe the mixing process. It assumes that the observed mixtures are linear combinations of the endmembers. Within an unsupervised framework, i.e., when both endmember signatures and abundances should be recovered, linear spectral unmixing can be formulated as the following minimization problem

$$\min_{\mathbf{M}, \mathbf{A}} \|\mathbf{Y} - \mathbf{M}\mathbf{A}\|_{\text{F}}^2 + \iota_{\mathbb{R}_+^{d_1 \times R_1}}(\mathbf{M}) + \iota_{\mathbb{S}_{R_1}^P}(\mathbf{A}) \quad (1)$$

where the matrices $\mathbf{Y} \in \mathbb{R}^{d_1 \times P}$ gathers all the observed pixels, $\mathbf{M} \in \mathbb{R}^{d_1 \times R_1}$ the endmembers, $\mathbf{A} \in \mathbb{R}^{R_1 \times P}$ the abundance vectors and $\iota_{\mathbb{R}_+^{d_1 \times R_1}}(\cdot)$ and $\iota_{\mathbb{S}_{R_1}^P}(\cdot)$ are respectively indicator functions on the non-negative quadrant and the column-wise indicator function on the R_1 -dimensional probability

simplex denoted by \mathbb{S}_{R_1} . The non-negative constraint over \mathbf{M} is justified by the fact that endmember signatures are reflectance spectra and thus non-negative. The second indicator function enforces non-negative and sum-to-one constraints on the abundance vectors \mathbf{a}_p ($p = 1, \dots, P$) in order to interpret them as proportion vectors. It is worth noting that the sum-to-one constraint is sometimes disregarded since it has been argued that relaxing this constraint out offers a better adaptation to possible changes of illumination in the scene [18]. Due to the general ill-conditioning of the endmember matrix \mathbf{M} , the objective function underlying (1) is often granted with additional regularizations promoting expected properties of the solution. In particular, numerous works exploited the expected spatial behavior of the mixing coefficients to introduce spatial regularizations enforcing piecewise-constant [5], [8] or smoothly varying [3], [19] abundance maps, possibly driven by external knowledge [20]. Conversely, this work does not consider spatial information as a prior knowledge but rather proposes a decomposition model dedicated to the image spatial content, paving the way towards the concept of *spatial unmixing*. This contribution is detailed in what follows.

B. Spatial mixing model

As previously mentioned, this paper proposes to complement the conventional linear unmixing problem (1) with an additional data-fitting term accounting for spatial information already contained in the hyperspectral image. To do so, for sake of generality, we assume that the scene of interest is characterized by vectors of spatial features $\mathbf{s}_p \in \mathbb{R}^{d_2}$ describing the context around the corresponding hyperspectral pixel indexed by p . The features can be extracted from the hyperspectral image directly or from any other available image of any modality of the same scene, with possibly better spatial resolution. For instance, one possibility consists in generating a virtual panchromatic image associated with the scene by averaging the hyperspectral bands and defining the features as the panchromatic pseudo-observations in a prescribed neighborhood. As a proof-of-concept but without limitation, this is the approach followed in Sections IV and V dedicated to numerical experiments.

To capture common spatial patterns, akin to a so-called *spatial unmixing*, these P d_2 -dimensional spatial features vectors \mathbf{s}_p gathered in a matrix $\mathbf{S} \in \mathbb{R}^{d_2 \times P}$ are assumed to be linearly decomposed according to the following optimization problem

$$\min_{\mathbf{D}, \mathbf{U}} \|\mathbf{S} - \mathbf{D}\mathbf{U}\|_{\text{F}}^2 + \iota_{\mathbb{R}_+^{d_2 \times R_2}}(\mathbf{D}) + \iota_{\mathbb{S}_{R_2}^P}(\mathbf{U}) \quad (2)$$

where $\mathbf{D} \in \mathbb{R}^{d_2 \times R_2}$ is a dictionary matrix and $\mathbf{U} \in \mathbb{R}^{R_2 \times P}$ the corresponding coding matrix.

This model can be interpreted as a dictionary-based representation learning task [21]. It means that the image in the considered feature space can be decomposed as a sum of elementary patterns collected in the matrix \mathbf{D} of spatial signatures. The corresponding coding coefficients are gathered in \mathbf{U} . The non-negativity constraints are imposed to ensure an additive decomposition similarly to what is done in the context of non-negative matrix factorization [22]. Finally, without any

constraint on the norms of \mathbf{U} and \mathbf{D} , the problem would suffer from a scaling ambiguity between \mathbf{U} and \mathbf{D} . Additional sum-to-one constraints are thus imposed on the columns of \mathbf{U} . It is worth noting that a similar model was implicitly assumed in [23]–[25] where a single-band image acquired by scanning transmission electron microscopy is linearly unmixed by principal component analysis [26], independent component analysis [27], N-FINDR [28] or thanks to a deep convolutional neural networks. However, in these works, the spatial feature space is defined by the magnitude of a sliding 2D-discrete Fourier transform, which unlikely ensures the additivity, or at least linear separability, assumptions underlying the mixtures.

C. Coupling spatial and spectral mixing models

After defining the spatial and spectral mixing models, we propose to relate both models by a coupling term, ensuring a joint spatial-spectral unmixing of the hyperspectral image. In this work, the coupling term is chosen such that it links the two coding matrices \mathbf{A} and \mathbf{U} , corresponding to the *spectral* and *spatial* abundances, respectively. More precisely, the coupling is formulated as the following penalized least-square problem

$$\min_{\mathbf{B}, \mathbf{Z}} \left\| \begin{pmatrix} \mathbf{A} \\ \mathbf{U} \end{pmatrix} - \mathbf{B}\mathbf{Z} \right\|_{\text{F}}^2 + \frac{\lambda_z}{2} \text{Tr}(\mathbf{Z}^T \mathbf{V} \mathbf{Z}) + \iota_{\mathbb{S}_K^P}(\mathbf{Z}) \quad (3)$$

with $\mathbf{V} = \mathbf{1}_K \mathbf{1}_K^T - \mathbf{I}_K$ where \mathbf{I}_K is the $K \times K$ identity matrix, $\mathbf{1}_K$ is the $K \times 1$ vector of ones and $\text{Tr}(\cdot)$ is the trace operator. This coupling term can be interpreted as a clustering task. The two coding matrices are concatenated and the clustering is then conducted on the columns of the resulting whole coding matrix. Centroids of the K clusters define the columns of the matrix $\mathbf{B} \in \mathbb{R}^{(R_1+R_2) \times K}$. Interestingly, each centroid is then the concatenation of a spatial signature and a spectral signature. In particular, it means that the pixels of a given cluster share the same spectral properties and a similar spatial context. Finally, the matrix $\mathbf{Z} \in \mathbb{R}^{K \times P}$ describes the assignments to the clusters, where \mathbf{z}_p gathers the probabilities of belonging to each of the clusters, hence the non-negativity and sum-to-one constraint enforced on it. It is accompanied with a specific regularization (see 2nd term of the right-hand side of (3)). This penalty promotes orthogonality over the lines of \mathbf{Z} since it can be rewritten as $\text{Tr}(\mathbf{Z}^T \mathbf{V} \mathbf{Z}) = \sum_{k_1 \neq k_2} \langle \mathbf{z}_{k_1}, \mathbf{z}_{k_2} \rangle$. This term becomes minimum when the assignments to clusters obey a hard decision, i.e., when one component of \mathbf{z}_p is equal to 1 and the others are set to 0. A strict orthogonality constraint would make the clustering problem equivalent to a k -means problem [29].

D. Joint spatial-spectral unmixing problem

Given the spectral mixing model recalled in Section II-A, the spatial mixing model introduced in Section II-B and their coupling term proposed in Section II-C, we propose to conduct

spatial-spectral unmixing jointly by considering the overall minimization problem

$$\begin{aligned} \min_{\mathbf{M}, \mathbf{A}, \mathbf{D}, \mathbf{U}, \mathbf{B}, \mathbf{Z}} & \frac{\lambda_0}{2} \|\mathbf{Y} - \mathbf{M}\mathbf{A}\|_{\text{F}}^2 + \iota_{\mathbb{R}_+^{d_1 \times R_1}}(\mathbf{M}) + \iota_{\mathbb{S}_{R_1}^P}(\mathbf{A}) \\ & + \frac{\lambda_1}{2} \|\mathbf{S} - \mathbf{D}\mathbf{U}\|_{\text{F}}^2 + \iota_{\mathbb{R}_+^{d_2 \times R_2}}(\mathbf{D}) + \iota_{\mathbb{S}_{R_2}^P}(\mathbf{U}) \\ & + \frac{\lambda_2}{2} \left\| \begin{pmatrix} \mathbf{A} \\ \mathbf{U} \end{pmatrix} - \mathbf{B}\mathbf{Z} \right\|_{\text{F}}^2 + \frac{\lambda_z}{2} \text{Tr}(\mathbf{Z}^T \mathbf{V} \mathbf{Z}) \\ & + \iota_{\mathbb{R}_+^{(R_1+R_2) \times K}}(\mathbf{B}) + \iota_{\mathbb{S}_K^P}(\mathbf{Z}) \end{aligned} \quad (4)$$

where λ_0 , λ_1 and λ_2 adjust the respective contribution of the various fitting terms. It is worth noting that, thanks to the sum-to-one constraints enforced on the spectral abundance vectors \mathbf{a}_p and spatial abundance vectors \mathbf{u}_p , all these coding vectors have the same unitary ℓ_1 -norm. It has the great advantage of avoiding a reweighing of the \mathbf{A} and \mathbf{U} in the coupling term regardless of the number of endmembers and dictionary atoms. However, it is still necessary to adjust the three parameters λ to weigh the various contribution terms. The strategy used in the experimental sections is to simply ensure that all terms as a similar weight by taking into account the size and dynamic of the involved matrices. The next section describes the optimization scheme adopted to solve the joint spatial-spectral unmixing problem (4).

III. OPTIMIZATION SCHEME

A. PALM algorithm

The cofactorization problem (4) is a non-convex, non-smooth optimization problem. For these reasons, the problem remains very challenging to solve and requires the use of advanced optimization tools. The choice has been made to resort to the proximal alternating linearized minimization (PALM) algorithm [30]. The core concept of PALM is to update each block of variables alternatively according to a proximal gradient descent step. This algorithm has the advantage to ensure the converge to a critical point of the objective function even in the case of a non-convex, non-smooth problem.

In order to obtain these convergence results, the objective function has to ensure a specific set of properties. Firstly, the various terms of the objective function have to be separable in a sum of one smooth term $g(\cdot)$ and a set of independent non-smooth terms. Then, each of the independent non-smooth term has to be a proper, lower semi-continuous function $f_i : \mathbb{R}^{n_i} \rightarrow (-\infty, +\infty]$. Finally, a sufficient condition is that the smooth term is a \mathcal{C}^2 -continuous function and that its partial gradients are globally Lipschitz with respect to the derivative variable. Further details are available in the original paper [30].

In problem (4), the smooth term $g(\cdot)$ is composed of the three quadratic terms and the orthogonality-promoting regularization. All these terms obviously verify the gradient Lipschitz and \mathcal{C}^2 -continuous properties. Moreover, the non-smooth terms f_i are separable into independent terms. Moreover, since they are all indicators functions on convex sets, their proximal operators are well-defined and, more specifically, are defined as the projection on the corresponding convex set. The projection on the non-negative quadrant is a simple thresholding of the

negative values and the projection on the probability simplex can be achieved by a simple sort followed by a thresholding as described in [31].

A summary of the overall optimization scheme is given in Algo. 1 where $L_{\mathbf{X}}$ stands for the Lipschitz constant of the gradient of $g(\cdot)$ considered as a function of \mathbf{X} . Partial gradients and Lipschitz moduli are all provided in Appendix A. Additional details regarding the implementation are discussed in what follows.

Algorithm 1: PALM

```

1 Initialize variables  $\mathbf{M}^0, \mathbf{A}^0, \mathbf{D}^0, \mathbf{U}^0, \mathbf{B}^0$  and  $\mathbf{Z}^0$ ;
2 Set  $\alpha > 1$ ;
3 while stopping criterion not reached do
4    $\mathbf{M}^{k+1} \in$ 
      $\text{prox}_{\mathbb{R}_+^{d_1 \times R_1}}^{\alpha L_{\mathbf{M}}} (\mathbf{M}^k - \frac{1}{\alpha L_{\mathbf{M}}} \nabla_{\mathbf{M}} g(\mathbf{M}^k, \mathbf{A}^k, \mathbf{D}^k, \mathbf{U}^k, \mathbf{B}^k, \mathbf{Z}^k));$ 
5    $\mathbf{A}^{k+1} \in$ 
      $\text{prox}_{\mathbb{S}_{R_1}^P}^{\alpha L_{\mathbf{A}}} (\mathbf{A}^k - \frac{1}{\alpha L_{\mathbf{A}}} \nabla_{\mathbf{A}} g(\mathbf{M}^{k+1}, \mathbf{A}^k, \mathbf{D}^k, \mathbf{U}^k, \mathbf{B}^k, \mathbf{Z}^k));$ 
6    $\mathbf{D}^{k+1} \in \text{prox}_{\mathbb{R}_+^{d_2 \times R_2}}^{\alpha L_{\mathbf{D}}} (\mathbf{D}^k -$ 
      $\frac{1}{\alpha L_{\mathbf{D}}} \nabla_{\mathbf{D}} g(\mathbf{M}^{k+1}, \mathbf{A}^{k+1}, \mathbf{D}^k, \mathbf{U}^k, \mathbf{B}^k, \mathbf{Z}^k));$ 
7    $\mathbf{U}^{k+1} \in \text{prox}_{\mathbb{S}_{R_2}^U}^{\alpha L_{\mathbf{U}}} (\mathbf{U}^k -$ 
      $\frac{1}{\alpha L_{\mathbf{U}}} \nabla_{\mathbf{U}} g(\mathbf{M}^{k+1}, \mathbf{A}^{k+1}, \mathbf{D}^{k+1}, \mathbf{U}^k, \mathbf{B}^k, \mathbf{Z}^k));$ 
8    $\mathbf{B}^{k+1} \in \text{prox}_{\mathbb{R}_+^{(R_1+R_2) \times K}}^{\alpha L_{\mathbf{B}}} (\mathbf{B}^k -$ 
      $\frac{1}{\alpha L_{\mathbf{B}}} \nabla_{\mathbf{B}} g(\mathbf{M}^{k+1}, \mathbf{A}^{k+1}, \mathbf{D}^{k+1}, \mathbf{U}^{k+1}, \mathbf{B}^k, \mathbf{Z}^k));$ 
9    $\mathbf{Z}^{k+1} \in \text{prox}_{\mathbb{S}_K^Z}^{\alpha L_{\mathbf{Z}}} (\mathbf{Z}^k -$ 
      $\frac{1}{\alpha L_{\mathbf{Z}}} \nabla_{\mathbf{Z}} g(\mathbf{M}^{k+1}, \mathbf{A}^{k+1}, \mathbf{D}^{k+1}, \mathbf{U}^{k+1}, \mathbf{B}^{k+1}, \mathbf{Z}^k));$ 
10 end
11 return  $\mathbf{M}^{\text{end}}, \mathbf{A}^{\text{end}}, \mathbf{D}^{\text{end}}, \mathbf{U}^{\text{end}}, \mathbf{B}^{\text{end}}, \mathbf{Z}^{\text{end}}$ 

```

B. Implementation details

Initialization and convergence – As explained, the PALM algorithm only ensures convergence to a critical point, i.e., a local minimum, of the objective function. Hence, it is important to have a good initialization of the variables to be estimated. In the following experiments, the initial end-member matrix \mathbf{M}^0 has been chosen as the output of the vertex component analysis (VCA) [32]. Abundance matrix is then initialized by solving the fully constrained least square problem $\min_{\mathbf{A} \in \mathbb{S}_{R_1}^P} \|\mathbf{Y} - \mathbf{M}\mathbf{A}\|_{\mathbb{F}}^2$. Finally, \mathbf{D}^0 and \mathbf{U}^0 are initialized by performing a k -means algorithm on columns of \mathbf{S} . Similarly \mathbf{B}^0 and \mathbf{Z}^0 are initialized by a k -means on the concatenation of \mathbf{U}^0 and \mathbf{A}^0 .

As stated in Algo. 1, a criterion is needed to monitor the convergence of the optimization algorithm. In the following experiments, the residual error of the objective function is computed at each iteration and, when the relative gap between the two last iterations is below a given threshold (10^{-4} for these experiments), the algorithm is stopped.

Hyperparameters – Several weighting coefficient λ have been introduced in problem (4) to adjust the respective contribution of each term. In the following experiments, some of these coefficients have been renormalized to take in consider-

ation the respective dimensions and dynamics of the matrices defining each term, yielding

$$\begin{cases} \lambda_0 &= \frac{1}{d_1 \|\tilde{\mathbf{Y}}\|_{\infty}^2} \tilde{\lambda}_0 \\ \lambda_1 &= \frac{1}{d_2 \|\tilde{\mathbf{S}}\|_{\infty}^2} \tilde{\lambda}_1 \end{cases} . \quad (5)$$

IV. EXPERIMENTS USING SIMULATED DATA

Performance of the proposed spatial-spectral unmixing method has been assessed thanks to experiments conducted on both synthetic and real data. The use of synthetic data makes quantitative validation possible whereas it is not possible with real data since there is no reference data.

A. Data generation

In order to properly evaluate the relevance of the proposed model, two synthetic images referred to as Image 1 and Image 2 have been generated such that they incorporate consistent spatial and spectral information. For this reason, the first step of the image synthesis consists in generating two so-called segmentation maps which separate the images into J regions. In this work, for each image, the segmentation maps has been randomly generated according to a Potts-Markov random field [33].

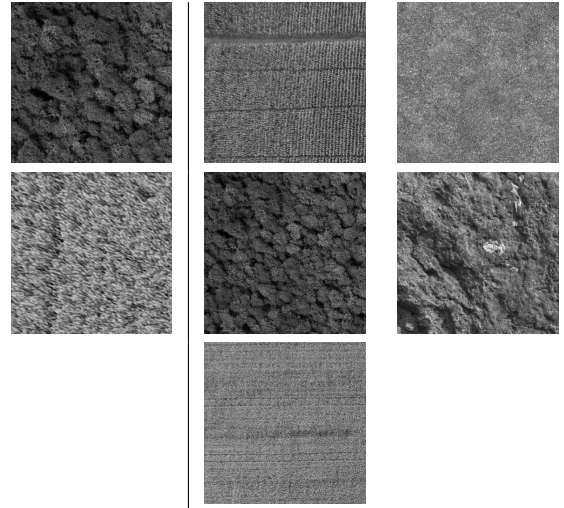


Figure 1. Synthetic dataset: textures (forest, wheat) for Image 1 (left) and textures (corn, grass, forest, rock, wheat) for Image 2 (right).

The second step is to assign specific spatial and spectral signatures to each area of the segmentation map. In order to get realistic images, grayscale textures are extracted from real remote sensing images and a distinct texture is assigned to each cluster of the segmentation. The textures are depicted in Fig. 1 for Image 1 and Image 2. Then, when the p th pixel belongs to the j th region ($j = 1, \dots, J$), its spectral abundance vector has been generated as the convex combination of two predefined extremal spectral behaviors $\psi_{i,1}$ and $\psi_{i,2}$ characterizing the j th region, i.e.,

$$\mathbf{a}_p = t_p^{(j)} \psi_{j,1} + (1 - t_p^{(j)}) \psi_{j,2} \quad (6)$$

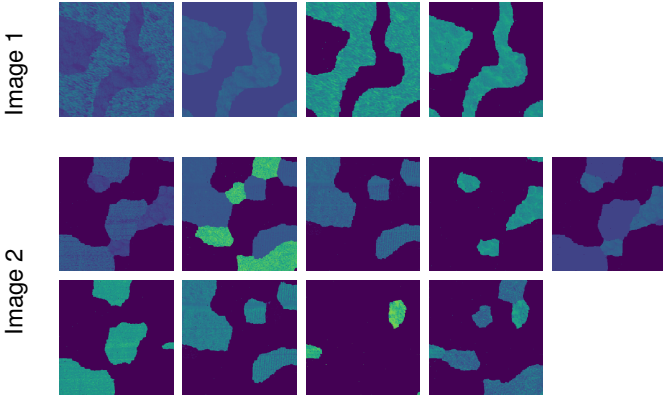


Figure 2. Synthetic dataset: abundance maps.

where $t_p^{(j)}$ is the intensity of the p th pixel of the j th grayscale texture. In other words, the texture intensity spatially modulates the spectral content differently in each region. The generated abundance maps are shown in Fig. 2.

The final step boils down to generating the hyperspectral image according to a linear mixing model. The endmember signatures have been extracted from the ASTER library. Two images have been generated according to this process. Image 1 is a 200×200 -pixel image composed of $R_1 = 4$ endmembers and $J = 2$ regions. Image 2 is a 300×300 -pixel image with $R_1 = 9$ endmembers and $J = 5$ regions. Additionally, corresponding panchromatic images are generated by normalizing and summing all spectral bands. The generated hyperspectral and panchromatic images are shown in Fig. 3.

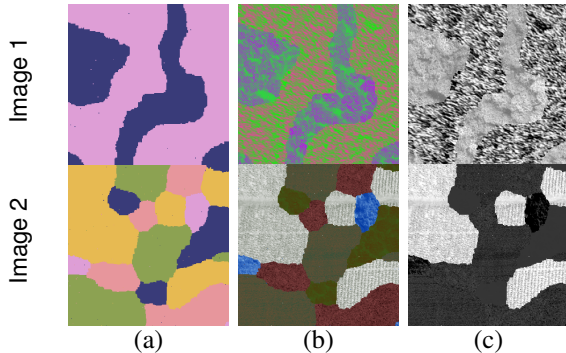


Figure 3. Synthetic dataset: (a) segmentation map, (b) color composition of the hyperspectral image, (c) panchromatic image.

B. Compared methods

In order to assess the performance of the proposed spatial-spectral unmixing model, referred to as SP2U, the unmixing results have been compared to several well-established methods. First, the result of the initialization method has been used as baseline. This method is conventional [2] and consists in extracting endmembers using VCA method [32] and then solving a fully constrained least square (FCLS) problem. This first method is referred to as VCA+FCLS hereafter.

The second compared method uses again a FCLS method to estimate the abundance vectors but uses an alternative endmember extraction algorithm. This method, called SISAL [34],

tries to estimate the minimum volume simplex containing the observed hyperspectral data by solving a non-convex problem using a splitting augmented Lagrangian technique.

The third compared method relies on a similar linear mixing model assumed by VCA+FCLS and SISAL+FCLS. However, instead of estimating the endmember signatures and abundances sequentially, it performs a joint estimation, yielding a non-negative matrix factorization (NMF) task with an additional sum-to-one constraint. This method referred to as NMF in the sequel, is a depreciated version of the SP2U problem (4) where $\lambda_1 = \lambda_2 = \lambda_z = 0$ and has been solved and initialized similarly.

The fourth method SUnSAL-TV was introduced in [5] and proposes to solve a conventional linear unmixing problem with an additional spatial regularization term to incorporate spatial information. The regularization term is chosen as a total variation applied to the abundance maps \mathbf{A} . It promotes in particular similarity of abundance vectors of neighboring pixels. In this case, the local information is used whereas SP2U method relates pixels sharing the same spatial context, akin to a non-local framework. It is important to note that this method does not estimate the endmember matrix which is estimated beforehand using VCA or SISAL.

The fifth method, denoted n-SP2U, is a naive counterpart of the proposed SP2U method. Instead of using the coupling term introduced in Section II-C, the abundance matrix \mathbf{A} and the coding coefficients \mathbf{U} are directly considered equal yielding the following problem

$$\min_{\mathbf{M}, \mathbf{A}, \mathbf{D}} \frac{\lambda_0}{2} \|\mathbf{Y} - \mathbf{M}\mathbf{A}\|_{\mathbb{F}}^2 + \iota_{\mathbb{R}_+^{d_1 \times R_1}}(\mathbf{M}) + \frac{\lambda_1}{2} \|\mathbf{S} - \mathbf{D}\mathbf{A}\|_{\mathbb{F}}^2 + \iota_{\mathbb{R}_+^{d_2 \times R_2}}(\mathbf{D}) + \iota_{\mathbb{S}_{R_1}^P}(\mathbf{A}). \quad (7)$$

This method is considered for comparison since it may come naturally to mind when willing to couple factorizations associated with spatial and spectral unmixing. However, it actually appears very unlikely to perform well in real scenarios. It would mean that the mixture proportions are always similar in the spatial and spectral domains. However a given spectral signal is obviously expected to appear in various spatial contexts. To account for distinct spatial patterns of a given spectral content, some endmembers would need to appear several times in the \mathbf{M} matrix, which is generally not a desired property.

C. Performance criteria

Performance of all methods has been assessed in term of endmember estimation using the average spectral angle mapper (aSAM)

$$\text{aSAM}(\mathbf{M}) = \frac{1}{R_1} \sum_{r=1}^{R_1} \arccos \left(\frac{\langle \mathbf{m}_r^{(\text{ref})} | \mathbf{m}_r \rangle}{\|\mathbf{m}_r^{(\text{ref})}\|_2 \|\mathbf{m}_r\|_2} \right), \quad (8)$$

and also in term of abundance estimation using the root mean square error (RMSE)

$$\text{RMSE}(\mathbf{A}) = \sqrt{\frac{1}{PR_1} \|\mathbf{A}^{(\text{ref})} - \mathbf{A}\|_{\mathbb{F}}^2}, \quad (9)$$

where $\mathbf{m}_r^{(\text{ref})}$ and \mathbf{A} are the r th actual endmember signature and the actual abundance matrix, respectively.

Two additional information have also been included in the results. The processing time includes the initialization, the endmembers extraction and the abundances estimation. Moreover we also consider the reconstruction error which measure how the model fits to the observed data

$$\text{RE} = \sqrt{\frac{1}{Pd_1} \|\mathbf{Y} - \mathbf{MA}\|_{\text{F}}^2}. \quad (10)$$

D. Results

As stated in Section II-B, the spatial feature matrix \mathbf{S} has been generated using the panchromatic image. For each pixel, the spatial feature vector is directly obtained by concatenating the values of the pixels in a 11×11 -pixel neighborhood around the considered pixel. This choice is very basic but designing the best spatial feature is out of the scope of this paper. Moreover, this choice has the advantage of offering a direct interpretation of the spatial content and cluster centroids as small 11-by-11 pixels images. For these experiments, the actual number of endmembers has been assumed known and thus $R_1 = 4$ for Image 1 and $R_1 = 9$ for Image 2. The number of dictionary atoms and clusters have been empirically adjusted and set such that $R_2 = 20$ and $K = 30$ for Image 1 and $R_2 = 30$ and $K = 40$ for Image 2. It is worth noting that increasing these two parameters tends to improve the performance up to a certain point where a slow decreasing can be observed. Hence, the choice of these values is not critical as long as they are high enough. It can be explained by the fact that a sufficient number of atoms and centroids is needed to explain the data. However, beyond a certain value, increasing these parameters reduces the regularization induced by the clustering. In a more general case, using features more robust to rotation and translation deformation would likely allow to reduce the number of needed clusters and dictionary atoms. Moreover, the weighting terms of the various methods have been adjusted manually using a gridsearch algorithm in order to obtain consistent results. In particular, weighting coefficients of SP2U method have been set to $\lambda_0 = \lambda_1 = \lambda_2 = 1.0$ and $\lambda_z = 0.1$.

As the solution of the considered problem suffers from a permutation ambiguity inherent to factor models, a reordering of the endmembers is thus necessary before any evaluation. In this experiment, this relabeling is performed such that the aSAM is minimum. The quantitative results, averaged over 10 trials, has then been computed for Image 1 and Image 2 and are presented respectively in Tables I and II.

The first conclusion of these results is that SP2U method gives the best estimation of the endmember matrix. All other endmember extraction algorithms are clearly behind. In particular, from Fig. 4, we can see that SP2U is the only method identifying that there are two spectra very different from the others which corresponds to the two soil spectra. Another interesting remark is that the NMF model barely improves the initializing point given by VCA+FCLS. It appears to converge in a few iteration to a local minimum close to initialization. Overall, it seems that including the spatial information allows

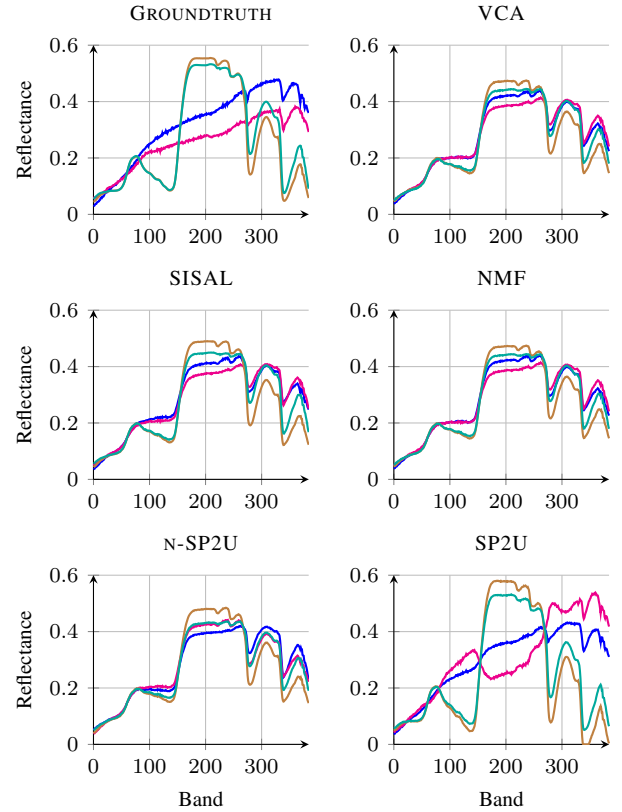


Figure 4. Image 1: estimated endmembers.

to identify more clearly the endmembers in particular in the considered case where the pure pixel assumption does not hold.

Then, regarding the estimation of abundances, the evaluation is less straightforward since it depends on the estimation of the endmembers. RMSE is computed after the reordering of the endmembers and, for Image 1, the best abundance maps are obtained with SISAL+FCLS but they are not associated with the best estimated set of endmembers. The case of Image 2 is easier to discuss since the best abundance maps, obtained by SP2U, are associated with the best set of endmembers. It is also interesting to consider a qualitative evaluation of the obtained abundance maps depicted in Fig. 5. Even if the quantitative results seem to support the quality of the abundance maps retrieved by SUnSAL-TV, the results visually appear overly smooth. On the other hand, abundance maps estimated by SP2U seem visually relevant but the corresponding RMSE suffers from an overestimation of abundances corresponding to soil spectra. Additionally, we can see that the RE is of the same order for every model except for n-SP2U. This means that all models are equally good at finding a mixture explaining the observed data excepted n-SP2U, which was expected as explained in Section IV-B. Some methods such as SISAL+FCLS get a slightly lower RE but it is mostly because the method is simply a direct minimization of the RE and it does not translate necessarily in a better RMSE. Finally, it is interesting to have a look at the computational times. SP2U appears as the slowest method since it inherits from a much richer model. However, the reported computational

Table I
IMAGE 1: QUANTITATIVE RESULTS (AVERAGED OVER 10 TRIALS).

Model	aSAM(M)	RE	RMSE(A)	Time (s)
VCA+FCLS	0.180 ($\pm 1.1 \times 10^{-2}$)	6.86×10^{-3} ($\pm 6.3 \times 10^{-3}$)	0.150 ($\pm 1.9 \times 10^{-2}$)	19 (± 11)
SISAL+FCLS	0.151 ($\pm 3.4 \times 10^{-3}$)	2.81×10^{-3} ($\pm 3.5 \times 10^{-6}$)	0.114 ($\pm 3.9 \times 10^{-3}$)	23 (± 0.1)
NMF	0.175 ($\pm 5.6 \times 10^{-3}$)	3.86×10^{-3} ($\pm 9.8 \times 10^{-4}$)	0.151 ($\pm 2.1 \times 10^{-2}$)	27 (± 29)
VCA+SUnSAL-TV	0.180 ($\pm 1.1 \times 10^{-2}$)	7.61×10^{-3} ($\pm 4.5 \times 10^{-3}$)	0.132 ($\pm 3.2 \times 10^{-2}$)	27 (± 0.1)
SISAL+SUnSAL-TV	0.151 ($\pm 2.9 \times 10^{-3}$)	4.6×10^{-3} ($\pm 1.1 \times 10^{-4}$)	0.0989 ($\pm 4.1 \times 10^{-3}$)	28 (± 0.3)
n-SP2U	0.188 ($\pm 1.5 \times 10^{-2}$)	28.1×10^{-3} ($\pm 1.2 \times 10^{-3}$)	0.192 ($\pm 9.6 \times 10^{-3}$)	93 (± 14)
SP2U	0.108 ($\pm 2.2 \times 10^{-2}$)	6.88×10^{-3} ($\pm 3.5 \times 10^{-4}$)	0.166 ($\pm 7.2 \times 10^{-2}$)	409 (± 38)

Table II
IMAGE 2: QUANTITATIVE RESULTS (AVERAGED OVER 10 TRIALS).

Model	aSAM(M)	RE	RMSE(A)	Time (s)
VCA+FCLS	0.176 ($\pm 5.8 \times 10^{-3}$)	8.80×10^{-3} ($\pm 2.2 \times 10^{-3}$)	0.246 ($\pm 4.2 \times 10^{-3}$)	100 (± 27)
SISAL+FCLS	0.187 ($\pm 1.7 \times 10^{-2}$)	4.61×10^{-3} ($\pm 5.0 \times 10^{-6}$)	0.145 ($\pm 2.3 \times 10^{-2}$)	57 (± 0.5)
NMF	0.178 ($\pm 5.9 \times 10^{-3}$)	4.87×10^{-3} ($\pm 6.3 \times 10^{-3}$)	0.246 ($\pm 4.2 \times 10^{-3}$)	109 (± 26)
VCA+SUnSAL-TV	0.176 ($\pm 5.8 \times 10^{-3}$)	9.48×10^{-3} ($\pm 6.4 \times 10^{-4}$)	0.229 ($\pm 3.6 \times 10^{-3}$)	81 (± 0.7)
SISAL+SUnSAL-TV	0.189 ($\pm 9.6 \times 10^{-3}$)	4.74×10^{-3} ($\pm 5.4 \times 10^{-5}$)	0.131 ($\pm 1.2 \times 10^{-2}$)	81 (± 2)
n-SP2U	0.190 ($\pm 1.8 \times 10^{-2}$)	35.3×10^{-3} ($\pm 4.1 \times 10^{-3}$)	0.212 ($\pm 3.0 \times 10^{-2}$)	518 (± 77)
SP2U	0.155 ($\pm 1.4 \times 10^{-2}$)	9.74×10^{-3} ($\pm 4.3 \times 10^{-4}$)	0.125 ($\pm 3.9 \times 10^{-2}$)	1174 (± 62)

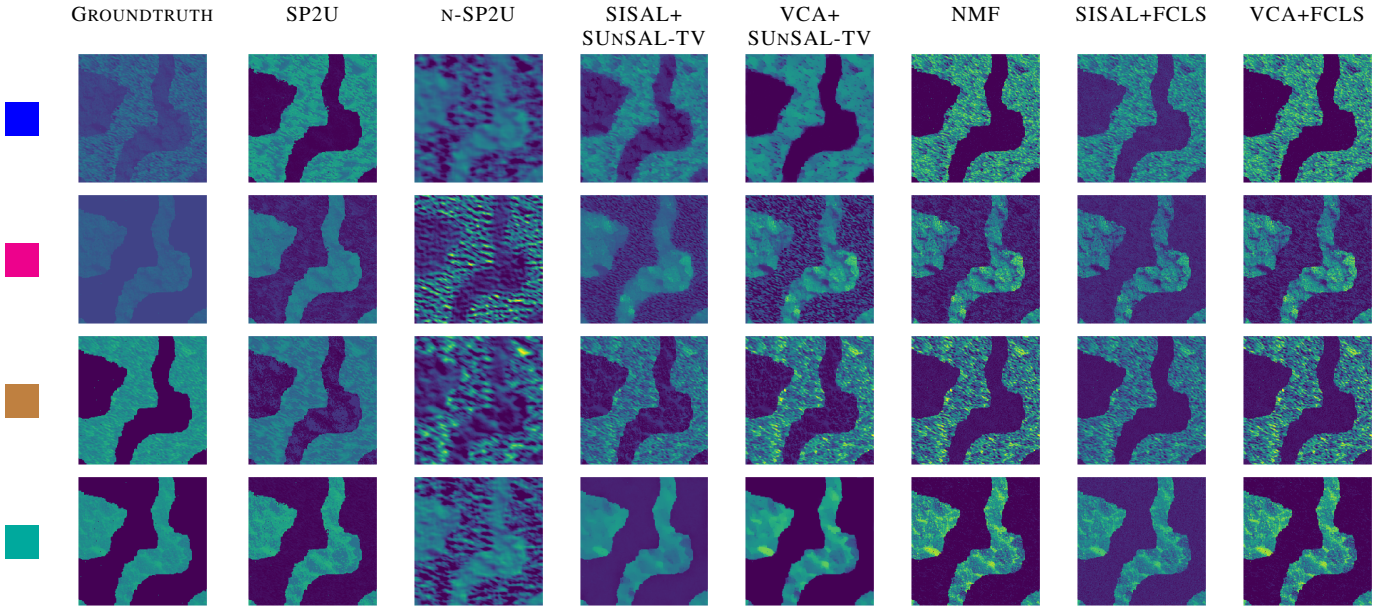


Figure 5. Image 1: abundance maps (the colored squares refer to the colors used to plot endmembers in Fig. 4).

times should be taken cautiously. Indeed, SUnSAL-TV and SISAL+FCLS were implemented with a fixed number of iterations and are based on Lagrangian augmented splitting methods. Conversely, other methods use a PALM algorithm with a different stopping criterion (see Section III-B).

V. EXPERIMENTS USING REAL DATA

A. Real dataset

The real aerial hyperspectral image used to conduct the following experiment was acquired by AVIRIS in 2013 on a site called Citrus Belt 3, California. The image is composed of 224 spectral bands from 400 to 2500 nanometers with a spatial resolution of 3m per pixel. After removing bands

corresponding to water absorption, a 751×651 -pixel image with $d_1 = 175$ spectral bands has been finally obtained. A panchromatic image of the scene is computed by normalizing then summing all spectral bands. The resulting image and a color composition of the scene are presented in Fig. 6. It is possible to state that the scene includes a desert area and several vegetation areas. Thus several soil and vegetation spectra are expected to be identified.

B. Compared methods

As explained in Section II, it is common to consider a sum-to-one constraint for abundance vectors to interpret them as proportion vectors. However, this assumption is not always fulfilled in practical scenarios. In the specific case of the



Figure 6. AVIRIS image: color composition of hyperspectral image (left) and corresponding panchromatic image (right).

considered AVIRIS image, we decide to drop this constraint due to important illumination variation in the image. For example, the desert area on the upper part of the image is a hill and the spectrum energy is almost doubled on its sunny side. In order to get a well-defined problem after dropping the sum-to-one constraint, it is necessary to introduce a new constraint such that there is no scaling ambiguity between \mathbf{M} and \mathbf{A} . The choice has been made to enforce a unit norm of the endmember spectra. Thus, the initial sum-to-one constraint was moved from columns of \mathbf{A} to columns of \mathbf{M} . Then, to get abundance maps summing to one, it is possible to normalize the obtained solution a posteriori. Similarly the sum-to-one was removed for SUnSAL-TV, n-SP2U and NMF. Moreover, similarly to the synthetic case, parameters of the problem have been adjusted manually and set to $\tilde{\lambda}_0 = \tilde{\lambda}_1 = \lambda_2 = 1$ and $\lambda_z = 0.1$, $R_1 = 6$, $R_2 = 20$ and $K = 30$.

C. Results

Since no groundtruth is available for this dataset only qualitative evaluations of the various methods are performed. First, Fig. 7 shows the endmembers estimated by all compared methods. As explained in the previous paragraph, endmembers have been normalized except for SISAL and VCA. Regarding SISAL results, it is possible to note that the method estimates endmember signatures taking negative values. Negative endmembers can not be interpreted as real reflectance spectra and SISAL thus appears the worst compared methods. This method tries to identify a minimum volume simplex containing the observations under the assumption that the observations belong to a $(R_1 - 1)$ -dimensional affine set. Thus, these poor results could be explained by a high noise level or non-linear mixtures. It is difficult to objectively compare the results of the other methods. However, the result obtained with SP2U method seems consistent with the visual content of the image since we can clearly identify *i*) two vegetation spectra (plotted in pink and orange) with strong absorbance in the visible domain and strong reflectance in the near-infrared domain [35] *ii*) two soil spectra (plotted in blue and brown) with an increase of the reflectance from $0.4\mu\text{m}$ to $1\mu\text{m}$ [36].

Regarding the abundance maps presented in Fig. 8, it seems again that the maps produced by SP2U are consistent with the actual content of the scene. They are in particular spatially

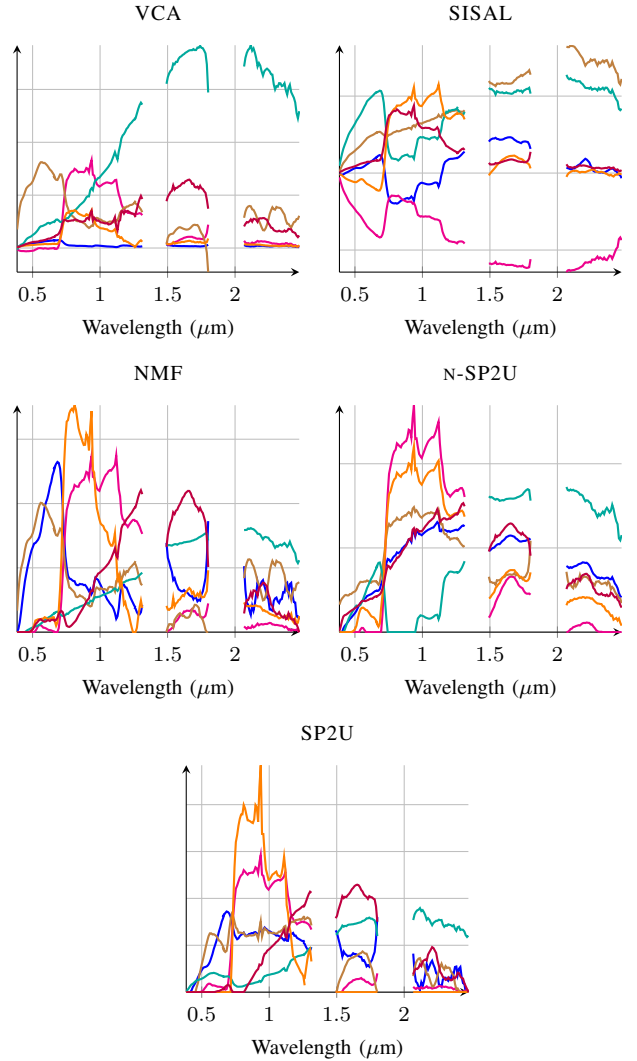


Figure 7. AVIRIS image: estimated endmembers. Note that endmembers estimated by NMF, n-SP2U and SP2U have been normalized to avoid scaling ambiguity intrinsic of the estimation method.

consistent with natural edges in the image. Additionally, SP2U results seem to be sparse in the sense that only a few endmembers are used for a given pixel while other methods recover very similar abundance maps with all endmembers, see, e.g., VCA+SUnSAL-TV. From Table III, it seems that ensuring the sum-to-one constraint makes more difficult to fit to the observations since VCA+FCLS has the highest RE. And, again as expected, SP2U method remains the slowest due to the overload of data to manipulate.

Besides, SP2U is not uniquely a spectral unmixing method and provides much richer interpretation. In Fig. 9, the results of the clustering performed by the coupling term are displayed. In particular, this figure shows the spatial position of the clusters, the spatial pattern characterizing the clusters and the mean spectra of the clusters. In this example, the first three clusters correspond to soil areas whereas the last two are vegetation, more precisely trees. For instance, the recovered spatial patterns associated with soil are smoother when the wooded areas are characterized by variations of higher frequencies.

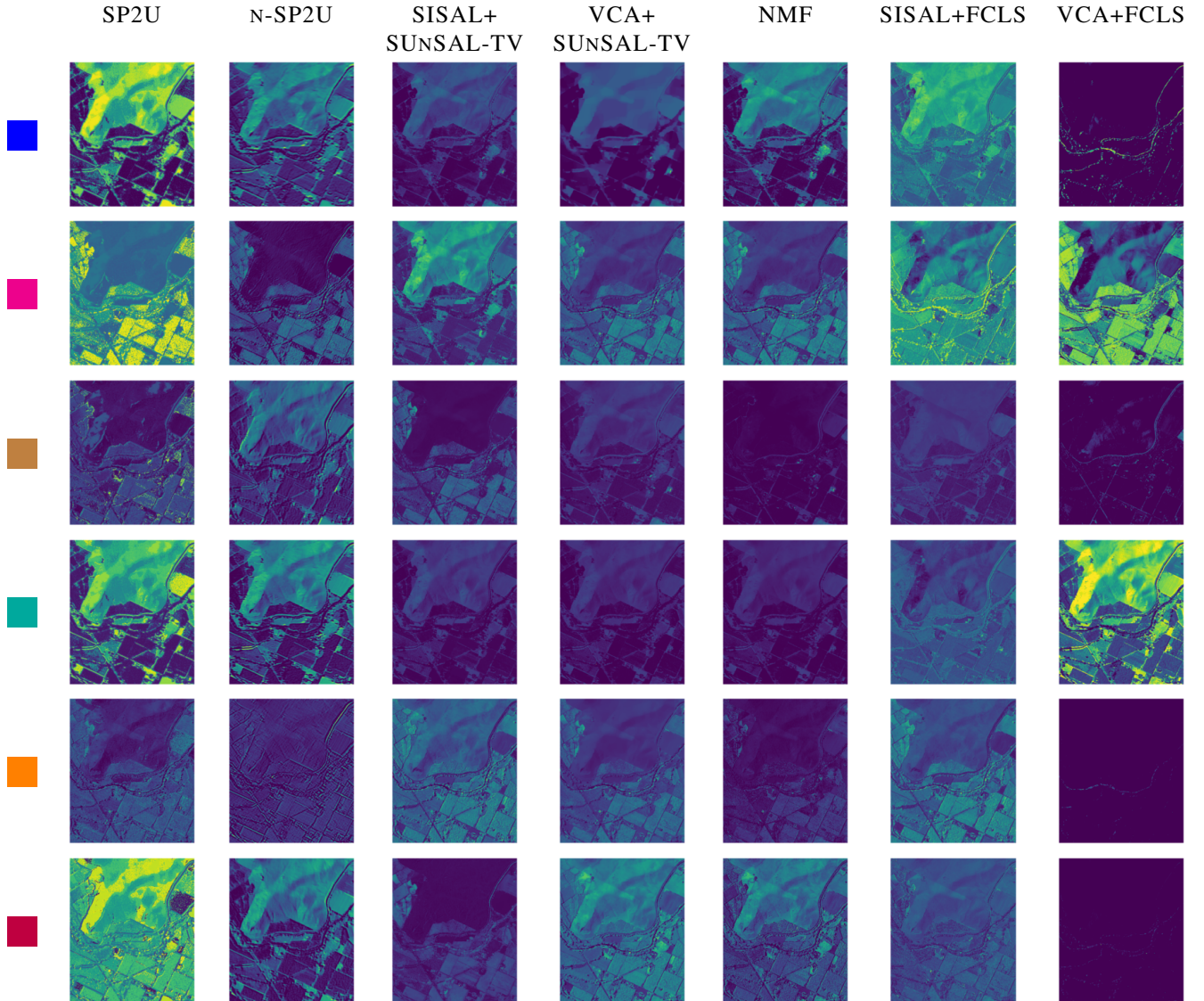


Figure 8. AVIRIS image: estimated abundance maps. The colored squares refer to the colors used to plot endmembers in Fig. 7. However, no reordering has been performed, i.e., endmembers have no particular relationship between methods.

Table III
AVIRIS IMAGE: QUANTITATIVE RESULTS.

Model	RE	Time (s)
VCA+FCLS	2.8×10^{-3}	12
SISAL+FCLS	0.14×10^{-3}	214
NMF	0.13×10^{-3}	2054
VCA+SUNSAI-TV	0.88×10^{-3}	471
SISAL+SUNSAI-TV	0.15×10^{-3}	455
n-SP2U	1.1×10^{-3}	1347
SP2U	1.4×10^{-3}	7162

VI. CONCLUSION AND PERSPECTIVES

This paper proposed a new model to interpret hyperspectral images. This method enriched the traditional spectral unmixing modeling by incorporating a spatial analysis of the data. Two data fitting terms, bringing respectively spectral and spatial information, were considered jointly, yielding a spatial-spectral

unmixing. This coupled learning process was made possible by the introduction of a clustering-driven coupling term linking the two coding matrices. This clustering process identified groups of pixels with similar spectral and spatial behaviors.

The experiments conducted on synthetic and real data showed that the proposed method performed very well both at identifying endmembers and estimating abundances. Moreover the relevance of this method was not limited to the unmixing results since the outputs of the clustering task were also of high interest. The identified clusters were characterized by their average spectral signature and spatial context.

To further explore the potential of the proposed model, it would be particularly interesting to investigate the use of more complex spatial features instead of using directly observations in a given neighborhood. For example, it would be relevant to use features more robust to rotation and translation in order to identify a texture instead of a fixed spatial pattern.

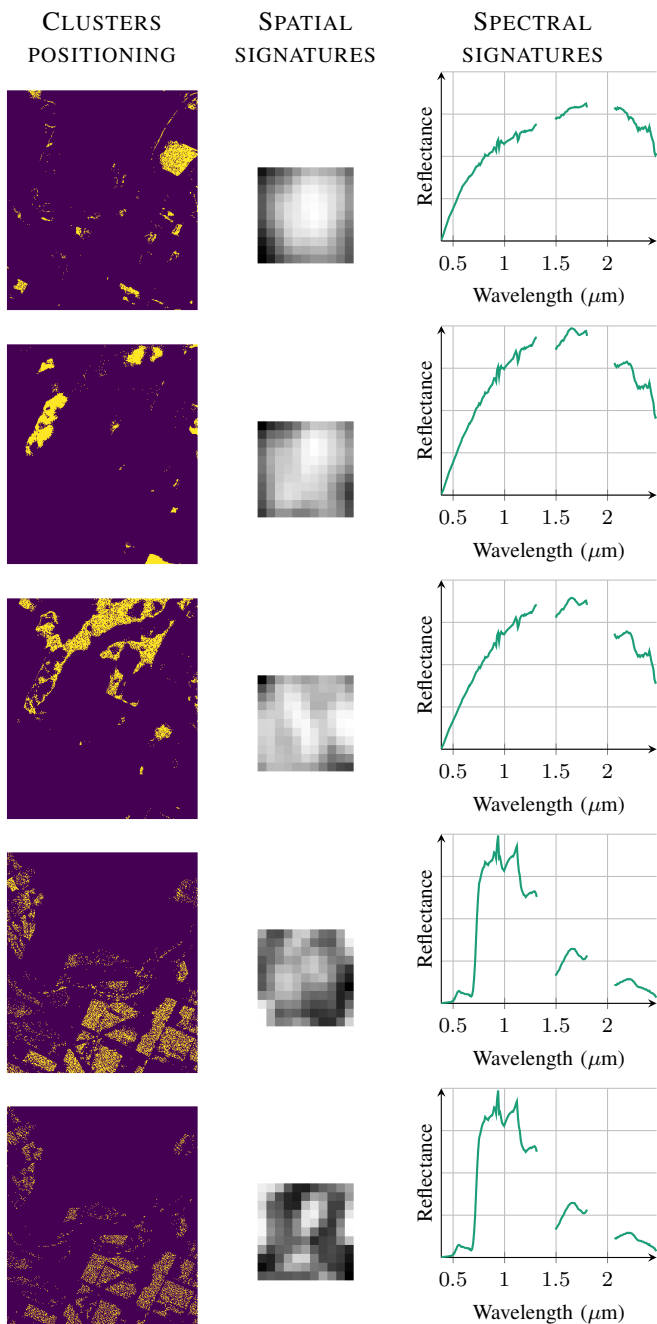


Figure 9. AVIRIS image: 5 particular clusters described by their spatial positioning (left), spatial signature (middle) and spectral signature (right).

APPENDIX

This appendix provides some details regarding the optimization schemes instanced for the proposed cofactorization model. Using notations adopted in Section III, the smooth coupling term can be expressed as

$$g(\mathbf{M}, \mathbf{A}, \mathbf{D}, \mathbf{U}, \mathbf{B}, \mathbf{Z}) = \frac{\lambda_0}{2} \|\mathbf{Y} - \mathbf{M}\mathbf{A}\|_{\mathbb{F}}^2 + \frac{\lambda_1}{2} \|\mathbf{S} - \mathbf{D}\mathbf{U}\|_{\mathbb{F}}^2 + \frac{\lambda_2}{2} \left\| \begin{pmatrix} \mathbf{A} \\ \mathbf{U} \end{pmatrix} - \mathbf{B}\mathbf{Z} \right\|_{\mathbb{F}}^2 + \frac{\lambda_z}{2} \text{Tr}(\mathbf{Z}^T \mathbf{V}\mathbf{Z}).$$

For a practical implementation of PALM, the partial gradients of $g(\cdot)$ and their Lipschitz moduli need to be computed

to perform the gradient descent. They are given by

$$\begin{aligned} \nabla_{\mathbf{M}}g(\mathbf{M}, \mathbf{A}, \mathbf{D}, \mathbf{U}, \mathbf{B}, \mathbf{Z}) &= \lambda_0(\mathbf{M}\mathbf{A}\mathbf{A}^T - \mathbf{Y}\mathbf{A}^T), \\ \nabla_{\mathbf{A}}g(\mathbf{M}, \mathbf{A}, \mathbf{D}, \mathbf{U}, \mathbf{B}, \mathbf{Z}) &= \lambda_0(\mathbf{M}^T\mathbf{M}\mathbf{A} - \mathbf{M}^T\mathbf{Y}) \\ &\quad + \lambda_2(\mathbf{A} - \mathbf{B}_1\mathbf{Z}), \\ \nabla_{\mathbf{D}}g(\mathbf{M}, \mathbf{A}, \mathbf{D}, \mathbf{U}, \mathbf{B}, \mathbf{Z}) &= \lambda_1(\mathbf{D}\mathbf{U}\mathbf{U}^T - \mathbf{S}\mathbf{U}^T), \\ \nabla_{\mathbf{U}}g(\mathbf{M}, \mathbf{A}, \mathbf{D}, \mathbf{U}, \mathbf{B}, \mathbf{Z}) &= \lambda_1(\mathbf{D}^T\mathbf{D}\mathbf{U} - \mathbf{D}^T\mathbf{S}) \\ &\quad + \lambda_2(\mathbf{U} - \mathbf{B}_2\mathbf{Z}), \\ \nabla_{\mathbf{B}}g(\mathbf{M}, \mathbf{A}, \mathbf{D}, \mathbf{U}, \mathbf{B}, \mathbf{Z}) &= \lambda_2(\mathbf{B}\mathbf{Z}\mathbf{Z}^T - \begin{pmatrix} \mathbf{A} \\ \mathbf{U} \end{pmatrix} \mathbf{Z}^T), \\ \nabla_{\mathbf{Z}}g(\mathbf{M}, \mathbf{A}, \mathbf{D}, \mathbf{U}, \mathbf{B}, \mathbf{Z}) &= \lambda_2(\mathbf{B}^T\mathbf{B}\mathbf{Z} - \mathbf{B}^T \begin{pmatrix} \mathbf{A} \\ \mathbf{U} \end{pmatrix}) \\ &\quad + \lambda_z\mathbf{V}\mathbf{Z} \end{aligned}$$

where \mathbf{B}_1 and \mathbf{B}_2 correspond to the submatrices of \mathbf{B} defined by the R_1 first rows and R_2 last rows, respectively, such that $\mathbf{B} = \begin{pmatrix} \mathbf{B}_1 \\ \mathbf{B}_2 \end{pmatrix}$.

All partial gradients are globally Lipschitz as functions of the corresponding partial variables. The following Lipschitz moduli can be explicitly derived as

$$\begin{aligned} L_{\mathbf{A}}(\mathbf{M}) &= \|\lambda_0\mathbf{M}^T\mathbf{M} + \lambda_2\mathbf{I}_{R_1}\|, \\ L_{\mathbf{M}}(\mathbf{A}) &= \|\lambda_0\mathbf{A}\mathbf{A}^T\|, \\ L_{\mathbf{U}}(\mathbf{D}) &= \|\lambda_1\mathbf{D}^T\mathbf{D} + \lambda_2\mathbf{I}_{R_2}\|, \\ L_{\mathbf{D}}(\mathbf{U}) &= \|\lambda_1\mathbf{U}\mathbf{U}^T\|, \\ L_{\mathbf{B}}(\mathbf{Z}) &= \|\lambda_2\mathbf{Z}\mathbf{Z}^T\|, \\ L_{\mathbf{Z}}(\mathbf{B}) &= \|\lambda_2\mathbf{B}^T\mathbf{B} + \lambda_z\mathbf{V}\|. \end{aligned} \quad (11)$$

REFERENCES

- [1] J. M. Bioucas-Dias, A. Plaza, N. Dobigeon, M. Parente, Q. Du, P. Gader, and J. Chanussot, "Hyperspectral Unmixing Overview: Geometrical, Statistical, and Sparse Regression-Based Approaches," *IEEE J. Sel. Topics Appl. Earth Observ. in Remote Sens.*, vol. 5, no. 2, pp. 354–379, 2012.
- [2] J. M. Bioucas-Dias and M. A. Figueiredo, "Alternating direction algorithms for constrained sparse regression: Application to hyperspectral unmixing," in *Proc. IEEE GRSS Workshop Hyperspectral Image Signal Process.: Evolution in Remote Sens. (WHISPERS)*. IEEE, 2010, pp. 1–4.
- [3] P.-A. Thouvenin, N. Dobigeon, and J.-Y. Tourneret, "Hyperspectral unmixing with spectral variability using a perturbed linear mixing model," *IEEE Trans. Signal Process.*, vol. 64, no. 2, pp. 525–538, 2015.
- [4] C. Shi and L. Wang, "Incorporating spatial information in spectral unmixing: A review," *Remote Sensing of Environment*, vol. 149, pp. 70–87, June 2014.
- [5] M.-D. Iordache, J. M. Bioucas-Dias, and A. Plaza, "Total Variation Spatial Regularization for Sparse Hyperspectral Unmixing," *IEEE Trans. Geosci. Remote Sens.*, vol. 50, no. 11, pp. 4484–4502, 2012.
- [6] S. Zhang, J. Li, H. C. Li, C. Deng, and A. Plaza, "Spectral-Spatial Weighted Sparse Regression for Hyperspectral Image Unmixing," *IEEE Trans. Geosci. Remote Sens.*, vol. 56, no. 6, pp. 3265–3276, June 2018.
- [7] X. Wang, Y. Zhong, L. Zhang, and Y. Xu, "Spatial Group Sparsity Regularized Nonnegative Matrix Factorization for Hyperspectral Unmixing," *IEEE Trans. Geosci. Remote Sens.*, vol. 55, no. 11, pp. 6287–6304, Nov. 2017.
- [8] O. Eches, N. Dobigeon, and J.-Y. Tourneret, "Enhancing hyperspectral image unmixing with spatial correlations," *IEEE Trans. Geosci. Remote Sens.*, vol. 49, no. 11, pp. 4239–4247, 2011.
- [9] O. Eches, J. A. Benediktsson, N. Dobigeon, and J.-Y. Tourneret, "Adaptive Markov random fields for joint unmixing and segmentation of hyperspectral image," *IEEE Trans. Image Processing*, vol. 22, no. 1, pp. 5–16, Jan. 2013.

- [10] K. Canham, A. Schlamm, A. Ziemann, B. Basener, and D. Messinger, "Spatially adaptive hyperspectral unmixing," *IEEE Trans. Geosci. Remote Sens.*, vol. 49, no. 11, pp. 4248–4262, 2011.
- [11] C. Deng and C. Wu, "A spatially adaptive spectral mixture analysis for mapping subpixel urban impervious surface distribution," *Remote Sens. Environ.*, vol. 133, pp. 62–70, June 2013.
- [12] D. R. Thompson, L. Mandrake, M. S. Gilmore, and R. Castano, "Superpixel endmember detection," *IEEE Trans. Geosci. Remote Sens.*, vol. 48, no. 11, pp. 4023–4033, 2010.
- [13] M. Zortea and A. Plaza, "Spatial preprocessing for endmember extraction," *IEEE Trans. Geosci. Remote Sens.*, vol. 47, no. 8, pp. 2679–2693, 2009.
- [14] C. Wang and D. M. Blei, "Collaborative topic modeling for recommending scientific articles," in *Proc. ACM SIGKDD Int. Conf. Knowledge Discovery Data Mining*, 2011, pp. 448–456.
- [15] J. Yoo, M. Kim, K. Kang, and S. Choi, "Nonnegative matrix partial co-factorization for drum source separation," in *Proc. IEEE Int. Conf. Acoust., Speech and Signal Process. (ICASSP)*, 2010, pp. 1942–1945.
- [16] N. Yokoya, T. Yairi, and A. Iwasaki, "Coupled nonnegative matrix factorization unmixing for hyperspectral and multispectral data fusion," *IEEE Trans. Geosci. Remote Sens.*, vol. 50, no. 2, pp. 528–537, 2012.
- [17] N. Akhtar and A. Mian, "Nonparametric Coupled Bayesian Dictionary and Classifier Learning for Hyperspectral Classification," *IEEE Trans. Neural Netw. Learn. Syst.*, vol. 29, no. 9, pp. 4038–4050, 2018.
- [18] L. Drumetz, M.-A. Veganzones, S. Henrot, R. Phlypo, J. Chanussot, and C. Jutten, "Blind hyperspectral unmixing using an extended linear mixing model to address spectral variability," *IEEE Trans. Image Process.*, vol. 25, no. 8, pp. 3890–3905, 2016.
- [19] S. Moussaoui, J. Idier, and E. Chouzenoux, "Alternating direction algorithms for constrained sparse regression: Application to hyperspectral unmixing," in *Proc. IEEE GRSS Workshop Hyperspectral Image Signal Process.: Evolution in Remote Sens. (WHISPERS)*. IEEE, June 2012.
- [20] T. Uezato, M. Fauvel, and N. Dobigeon, "Hyperspectral image unmixing with LiDAR data-aided spatial regularization," *IEEE Trans. Geoscience and Remote Sensing*, vol. 56, no. 2, pp. 4098–4108, July 2018.
- [21] M. Aharon, M. Elad, and A. Bruckstein, "K-SVD: An algorithm for designing overcomplete dictionaries for sparse representation," *IEEE Trans. Signal Process.*, vol. 54, no. 11, p. 4311, 2006.
- [22] D. D. Lee and H. S. Seung, "Learning the parts of objects by nonnegative matrix factorization," *Nature*, vol. 401, no. 6755, p. 788, 1999.
- [23] R. K. Vasudevan, A. Belianinov, A. G. Gianfrancesco, A. P. Baddorf, A. Tselev, S. V. Kalinin, and S. Jesse, "Big data in reciprocal space: Sliding fast fourier transforms for determining periodicity," *Appl. Phys. Lett.*, vol. 106, no. 9, p. 091601, 2015.
- [24] R. K. Vasudevan, M. Ziatdinov, S. Jesse, and S. V. Kalinin, "Phases and interfaces from real space atomically resolved data: Physics-based deep data image analysis," *Nano Lett.*, vol. 16, no. 9, pp. 5574–5581, 2016.
- [25] R. K. Vasudevan, N. Laanait, E. M. Ferragut, K. W. and David B. Geohegan, K. Xiao, M. Ziatdinov, S. Jesse, O. Dyck, and S. V. Kalinin, "Mapping mesoscopic phase evolution during e-beam induced transformations via deep learning of atomically resolved images," *npj Computational Materials*, vol. 4, 2018.
- [26] I. T. Jolliffe, *Principal Component Analysis*. New York: Springer-Verlag, 1986.
- [27] A. Hyvärinen, J. Karhunen, and E. Oja, *Independent Component Analysis*. New York: John Wiley, 2001.
- [28] M. E. Winter, "N-FINDR: an algorithm for fast autonomous spectral end-member determination in hyperspectral data," in *Proc. SPIE Imaging Spectrometry V*, M. R. Descour and S. S. Shen, Eds., vol. 3753, no. 1. SPIE, 1999, pp. 266–275.
- [29] F. Pompili, N. Gillis, P.-A. Absil, and F. Glineur, "Two algorithms for orthogonal nonnegative matrix factorization with application to clustering," *Neurocomputing*, vol. 141, pp. 15–25, 2014.
- [30] J. Bolte, S. Sabach, and M. Teboulle, "Proximal alternating linearized minimization for nonconvex and nonsmooth problems," *Mathematical Programming*, vol. 146, no. 1-2, pp. 459–494, Aug. 2014.
- [31] L. Condat, "Fast projection onto the simplex and the l_1 ball," *Math. Program.*, vol. 158, no. 1-2, pp. 575–585, 2016.
- [32] J. M. P. Nascimento and J. M. Bioucas-Dias, "Vertex component analysis: A fast algorithm to unmix hyperspectral data," *IEEE Trans. Geosci. Remote Sens.*, vol. 43, no. 4, pp. 898–910, April 2005.
- [33] S. Z. Li, *Markov Random Field Modeling in Image Analysis*. Springer Science & Business Media, 2009.
- [34] J. M. Bioucas-Dias, "A variable splitting augmented Lagrangian approach to linear spectral unmixing," in *2009 First Workshop on Hyperspectral Image and Signal Processing: Evolution in Remote Sensing*. IEEE, 2009, pp. 1–4.
- [35] R. B. Myneni, F. G. Hall, P. J. Sellers, and A. L. Marshak, "The interpretation of spectral vegetation indexes," *IEEE Trans. Geosci. Remote Sens.*, vol. 33, no. 2, pp. 481–486, 1995.
- [36] M. F. Baumgardner, L. F. Silva, L. L. Biehl, and E. R. Stoner, "Reflectance properties of soils," in *Advances in Agronomy*. Elsevier, 1986, vol. 38, pp. 1–44.